Hindawi
Advances in Civil Engineering
Volume 2023, Article ID 7881551, 13 pages
https://doi.org/10.1155/2023/7881551

Research Article

Cyclic Behavior of Square CFST Columns-Based Joint

Ruifeng Nie, Jinfeng Yao, Songhui Li, Shuo Wang, and Weiwei Han

Shandong Key Laboratory of Civil Engineering Disaster Prevention and Mitigation, Shandong University of Science and Technology, Qingdao 266590, China

Correspondence should be addressed to Weiwei Han; skd994504@sdust.edu.cn

Received 10 March 2023; Revised 25 July 2023; Accepted 1 September 2023; Published 1 November 2023

Academic Editor: Ying Qin

This paper investigates the cyclic behavior of six square concrete-filled steel tube (CFST) columns that take the effect of width–thickness ratio ($D/t = 30$, 40, and 60), slenderness ratio ($\lambda = 19.63$ and 24.25), and axial force ratio ($n = 0.6$, 0.4, and 0.2) into consideration. The failure modes, hysteretic behavior, energy dissipation capacities, stiffness degradation, and ductility of these specimens have been discussed and studied. The results revealed that a bigger D/t could reduce the energy dissipation capacities and bearing capacities of the columns. With increasing λ, the energy dissipation capacities and bearing capacities of columns reduced, and the stiffness deteriorated rapidly. The axial force ratio could enhance the bearing capacities but weaken their energy dissipation capacities and stiffness. Calculation formulae for ultimate moment strength of square CFST columns were exhibited to compare to the test results.

1. Introduction

Square concrete-filled steel tube (CFST) columns have commonly existed in bridges, underground infrastructures, industrial plants, and mansions with good bearing capacity and deformation capacity [1–3].

Researchers carried out experimental and numerical studies to investigate the bearing capacities of square CFST columns, they obtained great achievements. Ding et al. [4, 5] performed axial compression tests for eight square CFST end columns. They found that high-steel strength improved the bearing capacity of columns. Lee et al. [6] found that high-concrete compression strength increased the bending capacity and stiffness of the square CFST columns. Evirgen et al. [7] executed axial compression experiments of square CFST stub columns under different width–thickness ratios (D/t, range: 50–100). They reported that the D/t was the key to affect the confining effect between steel tubes and infill concrete. And a smaller width–thickness ratio could intensify the columns bearing capability. Yang et al. [8] investigated axial compression tests on square CFST columns. They found that a smaller width–thickness ratio could delay postpeak strength degradation. Parameter analysis was also conducted by the finite element models with different finite element analysis software. Ayough et al. [9] studied the axial compression behavior of CFST columns with ABAQUS. The results showed that high steel and concrete strength could significantly enhance the bearing capacities of CFST columns. Qasim [10] investigated CFST columns' axial compression performance by ANSYS. They found that the ultimate bearing capacity increased by 15.0% with decreasing D/t (range: 25–30). Qian and Jiang [11] developed a design approach for assessing axial bearing capacities of CFST composite columns. According to the unified strength theory, Yang et al. [8] proposed a formula to evaluate the bearing capacities of CFST columns with concrete strength from 70 to 150 MPa. Ke et al. [12] calculated and compared the bearing capacities of square CFST columns through unified strength and superposition theories. They found that calculation results by unified strength theory were more accurate. It indicated that material strength and width–thickness ratio were the main factors affecting the square CFST columns.

The cyclic behavior of CFST columns was also studied. Zhang and Gao [13] tested six square CFST columns under cyclic loading. The results showed that a smaller D/t could enhance the energy dissipation capacity, initial stiffness, and bearing capability of the CFST column. Silva et al. [14] carried out cyclic loading tests of square CFST columns, they

Table 1: Main information of specimens.

Specimens	Dimension of column section (mm)	Column height (mm)	Width–thickness ratio (D/t)	Slenderness ratio (λ)	Axial compression ratio (n)
No. 1	$300 \times 300 \times 5$	1,700	60	19.63	0.4
No. 2	$300 \times 300 \times 10$	1,700	30	19.63	0.4
No. 3	$300 \times 300 \times 7.5$	2,100	40	24.25	0.4
No. 4	$300 \times 300 \times 7.5$	1,700	40	19.63	0.2
No. 5	$300 \times 300 \times 7.5$	1,700	40	19.63	0.6
No. 6	$300 \times 300 \times 7.5$	1,700	40	19.63	0.4

found that the columns with smaller slenderness ratios had stronger energy dissipation capacity and bearing capability. Wang et al. [15] investigated the seismic performance on CFST columns connected to binding bars under the cyclic loadings and axial compression. They reported that a big axial force ratio could elevate the peak bearing capability and initial stiffness while weakening the energy dissipation capacity of the specimens. Chen et al. [16] tested six square CFST columns under cyclic loadings. They indicated that the high-axial force ratio increased the bearing capacity but accelerated the stiffness degradation. Parameter analysis were also conducted by the finite element analysis softwares. Zhou et al. [17] studied the seismic behavior of CFST columns by ABAQUS. The results revealed that the bearing capability of columns increased by 41%, and the ductility coefficient decreased by 30% with decreasing D/t (range: 58–100). Xu et al. [18] proposed the numerical model of square CFST columns with SeismoStruct. The parameter analysis showed that the specimen's ultimate bearing capacity improved and the ductility coefficient reduced with increasing steel strength. The cyclic behavior of square CFST columns with stiffeners was studied by Han et al. [19]. They proposed an equation to calculate the flexural capacity of columns considering the influence of the stiffeners. Based on the superposition theory and limit equilibrium theory, Ke et al. [20] proposed the estimation approach to assess the compressing–bending capacity of square CFST composite columns. Additionally, different configurations of column-based joints were also reported. The seismic performance of the proposed CFST column base joints was investigated by Mou et al. [21]. They found that axial force played a key role in improving the joints' flexural capacity. A special kind of exposed square CFST column base was presented by Qiao et al. [22]. They investigated the seismic performance of the bases and presented a calculating method to predict the interaction curve of bending moment versus axial force at the ultimate state.

The paper investigates the seismic behavior of square CFST columns. Six CFST columns were examined by the axial constant and horizontal cyclic loadings tests to systematically analyze the effects of three parameters (λ, D/t, and n). The failure modes, hysteresis performance, energy dissipation capacities, stiffness degradation, and ductility of specimens were discussed and analyzed. A calculating approach for evaluating ultimate flexural strength of the square CFST column was also proposed.

2. Experiments

2.1. Tested Specimens. Six square CFST columns have been manufactured for investigating the cyclic behavior. The main tested parameters included width–thickness ratio ($D/t = 30$, 40, and 60), slender ratio ($\lambda = 19.63$ and 24.25), and axial force ratio ($n = 0.2$, 0.4, and 0.6) (Table 1). The slender ratio and axial force ratio could be calculated according to Equations (1) and (2), respectively.

$$\lambda = 2\sqrt{3}L/D\,, \tag{1}$$

$$n = N/\left(A_s f_y + A_c f_c\right), \tag{2}$$

where D and L are the width and height of columns; N is the axial force on the column top exerted through the oil jack; f_y and A_s are the yield stress and cross-section area of a square steel tube, respectively; f_c and A_c are compressive strengths and cross-section area of the infilled concrete, separately.

Figure 1(a) shows the details of specimen No. 1 with height of 2,400 mm. The cross-sectional dimensions of a steel tube were $300 \times 300 \times 5$ mm (length × width × thickness), while the steel plate fixed at the steel tube bottom was $700 \times 500 \times 20$ mm (length × width × thickness) (Figure 1(b)). The RC foundation was $1{,}400 \times 700 \times 700$ mm (length × width × thickness) (Figure 1(c)).

2.2. Steel Properties. The steel tubes' mechanical properties were obtained from the coupon tests on standard specimens (Figure 2), according to the Standard GB/T 228.1-2010 [23]. The stress–strain relationship of the steel part is exhibited in Figure 3(a). Table 2 shows the steel properties, such as E_s (Young's modulus), f_y (yield stress), and f_t (tensile stress). The same concrete was used for the columns and foundations. Six concrete cubic specimens were tested in the reference to Standard GB/T 50081-2019 [24]. Figure 3(b) shows the stress–strain relationship of the concrete. Its corresponding axial compressive strength (f_c) equaled 23.3 MPa.

2.3. Test Apparatus. Figure 4 exhibits the test apparatus of square CFST columns. The RC foundation was fixed by pressure beams and anchor rods. An oil jack connected with a girder imposed the constant axial loading through sliding support. A 500 kN actuator applied the horizontal cyclic loadings to the column end.

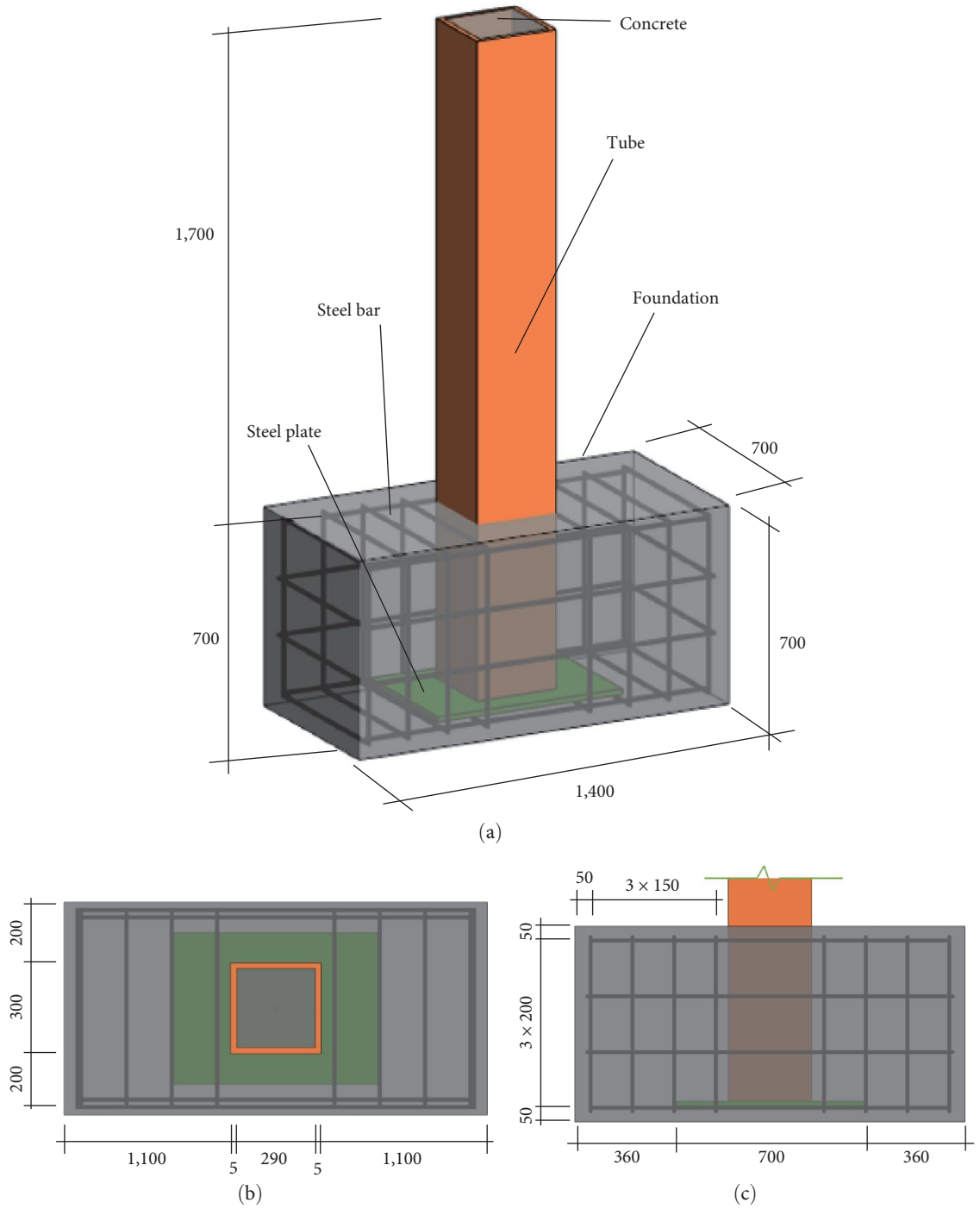

Figure 1: Schematic of specimen No. 1 (mm): (a) details of the specimen, (b) cross-section, and (c) steel bars arrangement.

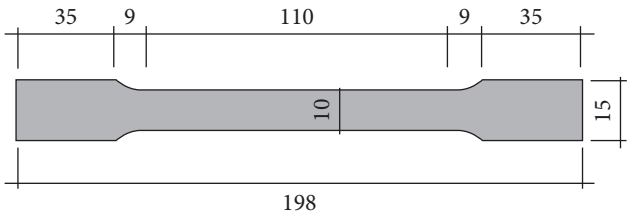

Figure 2: Dimensions of the coupon (mm).

The horizontal cyclic loading was conducted by the combined force–displacement controlling program [25] (Figure 5). P_y and Δ_y are the yield load and yield displacement. The column end pushed south was identified as the negative direction, and the other column end pulled north as the positive direction. The testing process was load control initially and the load was applied with the amplitude of 1/3 P_y, 2/3 P_y, and P_y step by step. Each loading level was cycled once. When the column yielded, the lateral load would be changed to a displacement-controlled program with an increment of Δ_y. Each loading level

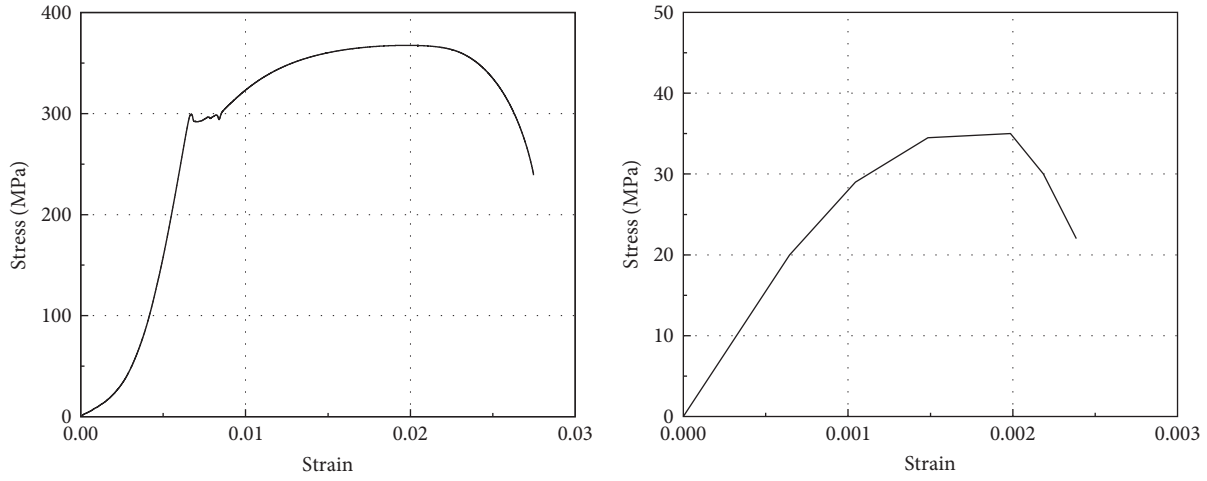

Figure 3: Stress–strain relation of materials: (a) Steel and (b) concrete.

Table 2: Material properties of steel parts.

Parts	Mechanical index		
	E_s (Mpa)	f_y (Mpa)	f_t (Mpa)
Square column	2.06×10^5	299.2	367.5

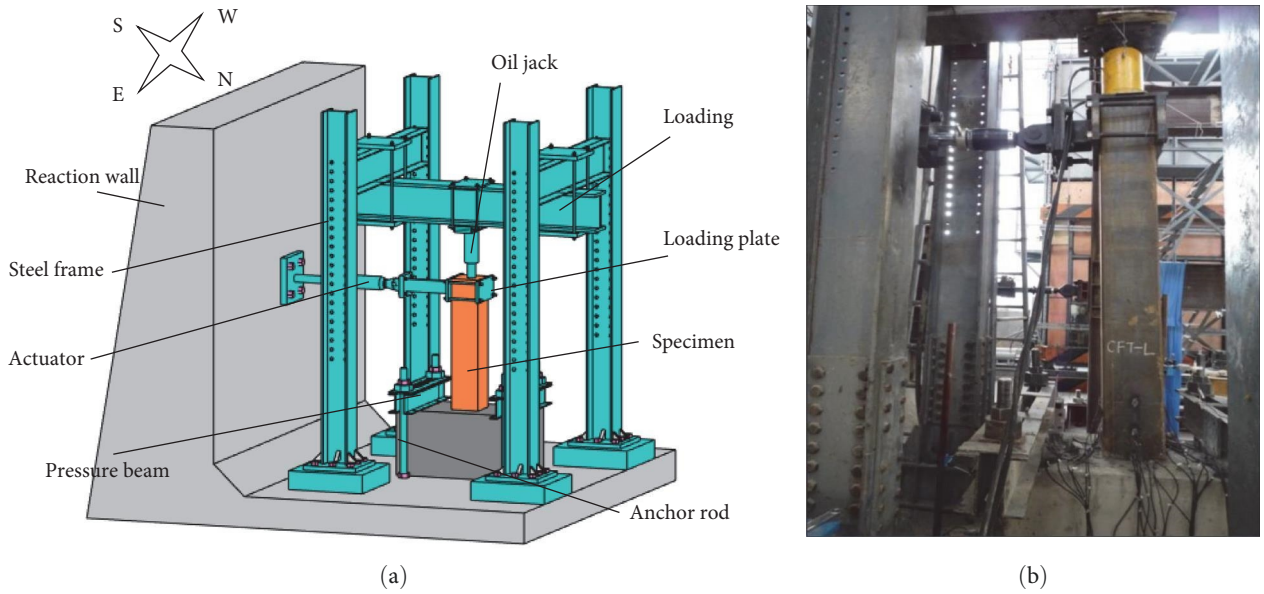

Figure 4: Test apparatus: (a) diagrammatic view and (b) photograph of test apparatus.

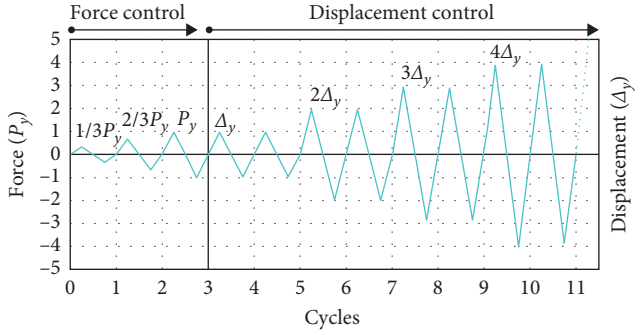

Figure 5: Loading program.

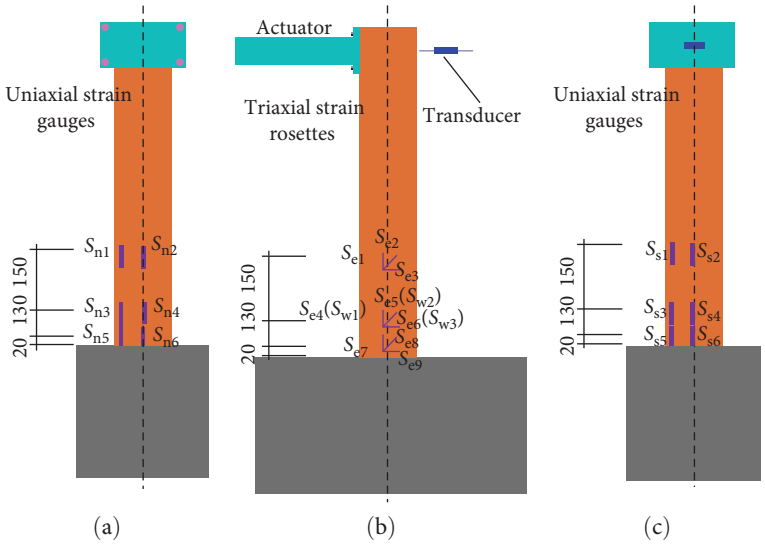

FIGURE 6: Arrangement of strain gauges and transducer: (a) north surface, (b) east surface, and (c) south surface.

was cycled twice. The loading process would be stopped until the lateral loadings reduced to 85% of the maximum loading.

2.4. Measurements. The strain of steel tubes was recorded by strain gauges (Figure 6). Three strain rosettes were pasted on the column in the east direction (S_e), 20, 150, and 300 mm far away from the RC surface, respectively. A strain rosette was stuck on the column in the west direction (S_w), 150 mm far away from the RC surface. Six strain gauges were stuck on the column in the north (S_n) and south (S_s) directions, respectively. The displacement and load information could be measured through the transducer in the actuator and checked by the transducer set at the column end (Figure 6(b)).

3. Result Analysis

3.1. Experimental Phenomenon. The failure modes of the six square CFST column specimens were similar (Figure 7). The failure of the six columns showed a compression–flexure failure mode. Table 3 lists the failure phenomenons in the tested process. The tested columns had no obvious change in the initial loading stage. After the yield point, the slight local buckling appeared on the north and south bottom of the steel tube successively. It was due to the compression and expansion of the infilled concrete during loading. As the lateral load increased, the local buckling became gradually severe. In addition, the local buckling also appeared on the east and west bottom of the steel tube. The lateral support devices in the test were not set, some specimens were stopped loading due to serious eccentric compression. The phenomenon of steel tube buckling in Specimen No. 5 occurred later than the other specimens. A higher axial compression ratio could alleviate the buckling of the steel tube. The weld cracking occurred at the steel tube corners of specimens No. 4 and No.5 (Figure 7(h) and 7(j)).

3.2. Hysteretic Performance. The relationships between the loading (P) and displacement (Δ) were illustrated in Figure 8. The maximum loading force (P_{max}) of all specimens appeared in the second loading level of the displacement-control program and was represented by the solid points in the figure.

As the width–thickness ratio (D/t) decreased, the P_{max} of Specimen No. 6 and No. 2 were increased by 31.8% and 60.0%, separately. In comparison to Specimen No. 1, the P_{max} of No. 6 was 32.5% higher than that of Specimen No. 3 due to the decrease in slenderness ratio (λ). Compared to Specimen No. 4, the P_{max} of Specimen No. 6 and No. 5 was increased by 9.9% and 12.1%, respectively. A larger axial compression ratio (n) showed a significant function in improving P_{max} of the square CFST columns.

3.3. Skeleton Curve and Main Performance Points. The skeleton diagrams of tested specimens with various parameters (D/t, λ, and n) are performed (Figure 9(a–c)), and the slope factor method (Figure 10) [21] was employed to determine the plastic and yield points. Table 4 lists the main performance points of the six specimens. As the width–thickness ratio decreased, the P_y and P_p of Specimen No. 1, No. 6, and No. 2 increased gradually. Compared with Specimen No. 3 and No. 6, a small slenderness ratio could improve the P_y and P_p of the square CFST columns. In Specimen No. 4–No. 6, the n has a limited impact on the P_y and P_p of the columns.

3.4. Stiffness Degradation. Stiffness degradation coefficient (K_j) can be calculated by Equation (3) as follows:

$$K_j = \sum_{i=1}^{N_c} P_{i,j} / \sum_{i=1}^{N_c} \Delta_{i,j}, \tag{3}$$

where $P_{i,j}$ is the peak loading force on the i-th hysteretic loop at the j-th phase; $\Delta_{i,j}$ is the displacement corresponding to $P_{i,j}$;; N_c is the amount of cycles.

Figure 11 demonstrates the stiffness degradation in six specimens. When Δ was smaller than 15 mm, the stiffness of each specimen had almost no degradation. The stiffness of

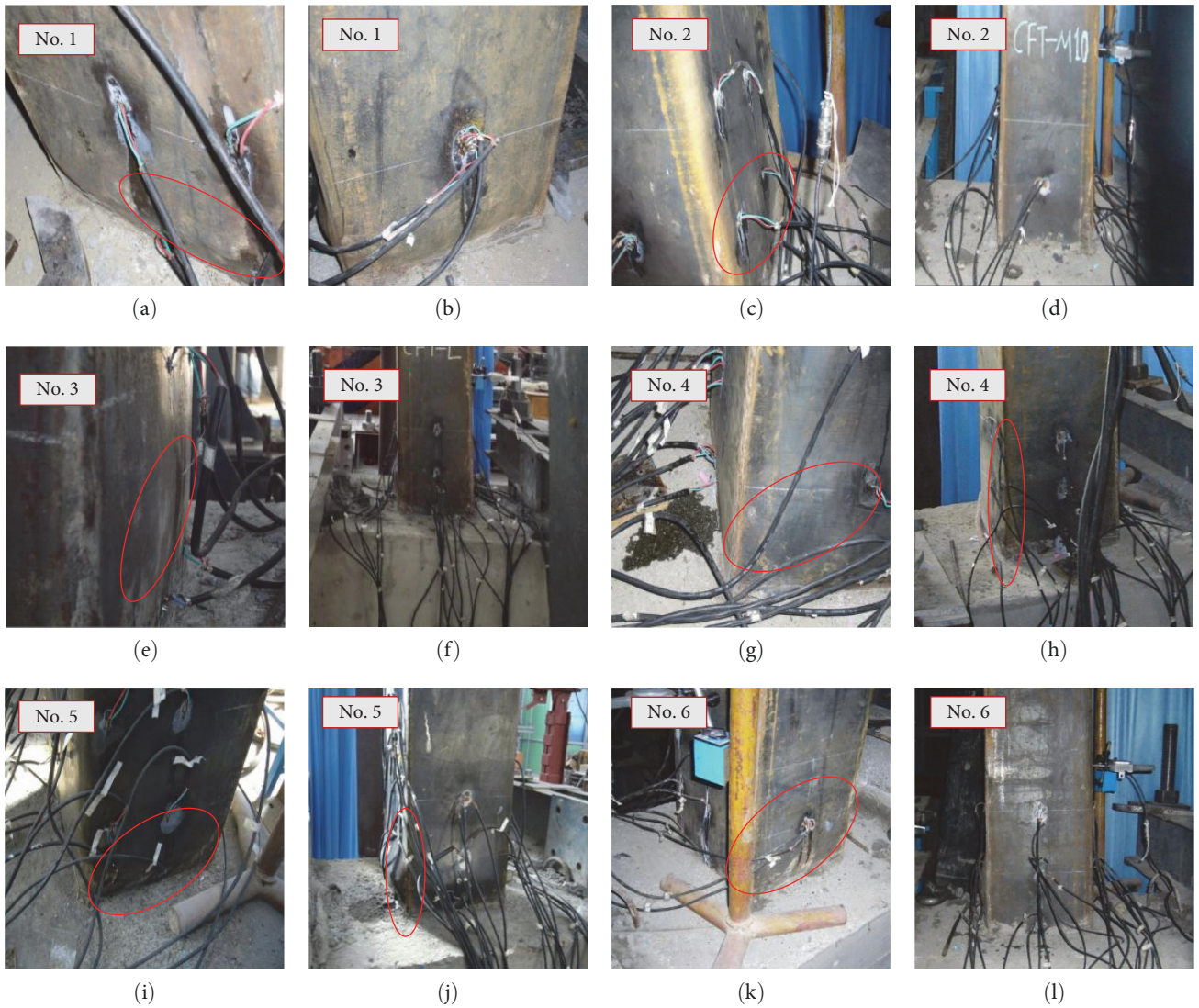

Figure 7: Failure modes of specimens: (a) local buckling, (b) final state, (c) local buckling, (d) final state, (e) local buckling, (f) final state, (g) local buckling, (h) final state, (i) local buckling, (j) final state, (k) local buckling, and (l) final state.

Table 3: Experimental phenomenon.

	No. 1	No. 2	No. 3	No. 4	No. 5	No. 6
$\Delta = \Delta_y$	Steel tube buckling (north)	–	–	Steel tube buckling (north)	–	–
$\Delta = 2\,\Delta_y$	Steel tube buckling (west, east)	Steel tube buckling (south, north)	Steel tube buckling (south, north)	Steel tube buckling (south)	–	Steel tube buckling (south, north)
$\Delta = 3\,\Delta_y$	Serious eccentric compression	Serious eccentric compression	Steel tube buckling (west, east)	Steel tube buckling (west, east)	Steel tube buckling (north, south)	Serious eccentric compression
$\Delta = 4\,\Delta_y$	–	–	Serious eccentric compression	Weld cracking	Steel tube buckling (west, east)	–
$\Delta = 5\,\Delta_y$	–	–	–	Concrete crushing	Weld cracking	–

Note: Δ_y of specimens No. 1–No. 6 are equal to 23.0, 31.0, 21.0, 38.0, 17.5, and 25.0 mm, respectively.

specimens decreased rapidly during the $\Delta = 15$–50 mm, and degraded slowly after $\Delta = 50$ mm. In attention, the stiffness of each specimen was different during the initial phase under two opposite directions. With increased load, the stiffness of each specimen under two loading directions degraded to the same level.

Table 5 lists the stiffness of specimens at the key performance points, the ratio of the stiffness between peak and

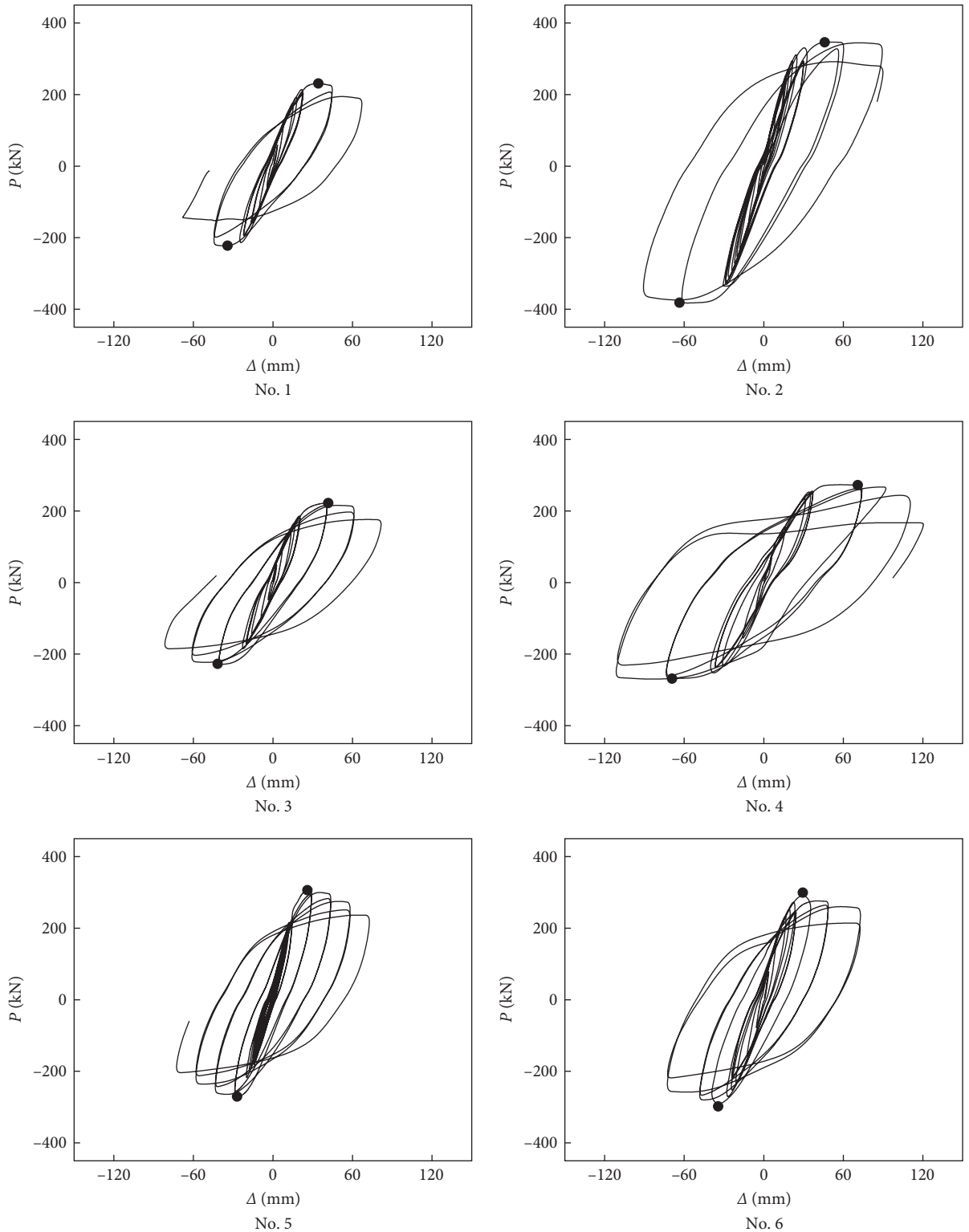

Figure 8: Hysteretic curves of $P-\Delta$.

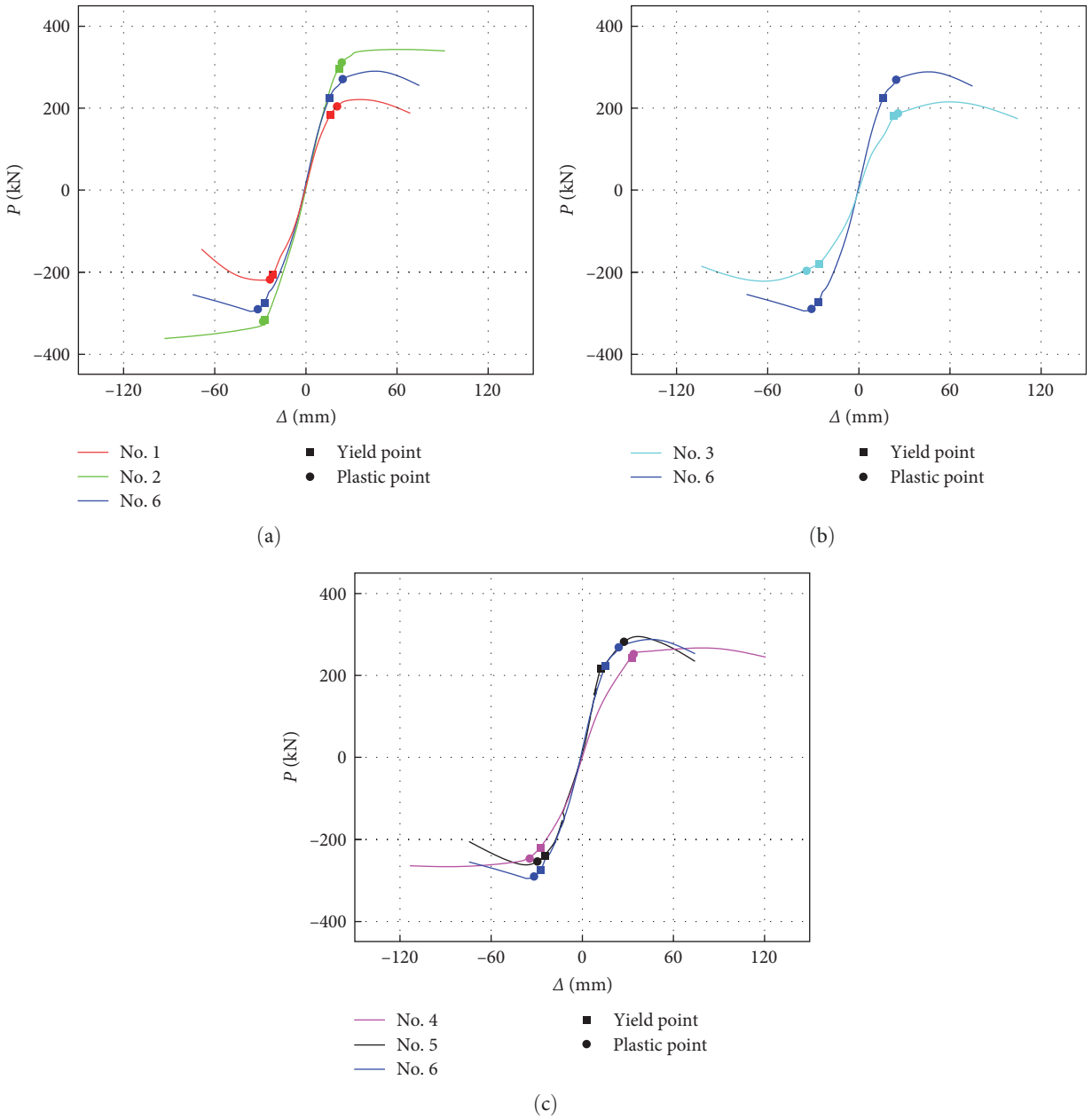

Figure 9: Comparison of skeleton curves: (a) width–thickness ratio, (b) slenderness ratio, and (c) axial compression ratio.

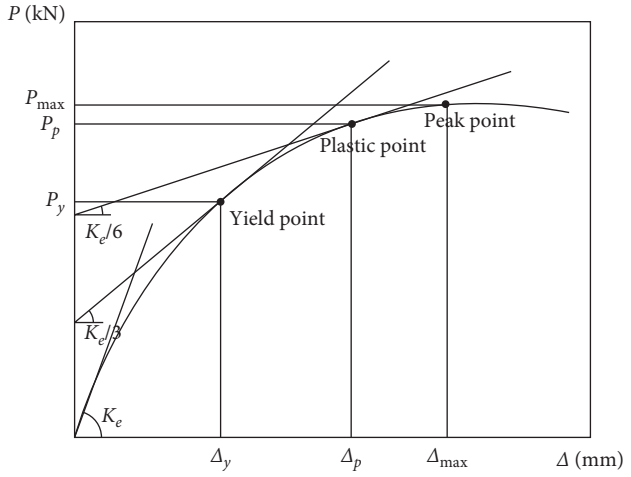

Figure 10: Definition of main performance points.

Table 4: Main performance points.

Specimen No.	Loading direction	K_e (kN/mm)	P_y (kN)	Δ_y (mm)	P_p (kN)	Δ_p (mm)	P_{max} (kN)	Δ_{max} (mm)
No. 1	Positive	17	184	16.3	204	20.6	231	43.7
	Negative	13	−206	−21.6	−218	−23.6	−223	−45.0
No. 2	Positive	18	296	21.9	311	23.7	345	60.6
	Negative	17	−316	−27.2	−320	−28.1	−382	−68.9
No. 3	Positive	14	182	22.6	188	25.5	222	52.8
	Negative	11	−181	−26.4	−197	−34.9	−229	−53.4
No. 4	Positive	13	244	32.8	254	34.1	273	84.4
	Negative	13	−220	−27.1	−247	−34.5	−269	−75.6
No. 5	Positive	16	217	12.8	284	27.8	306	30.0
	Negative	11	−239	−24.4	−254	−29.4	−271	−30.4
No. 6	Positive	21	225	15.5	270	24.3	299	48.9
	Negative	14	−275	−27.3	−290	−31.6	−298	−34.6

Note: K_e is initial stiffness, P_y is yield loading force, P_p is plastic loading force, P_{max} is maximum loading force, Δ_y is yield displacement, Δ_p is plastic displacement, and Δ_{max} is displacement of P_{max}.

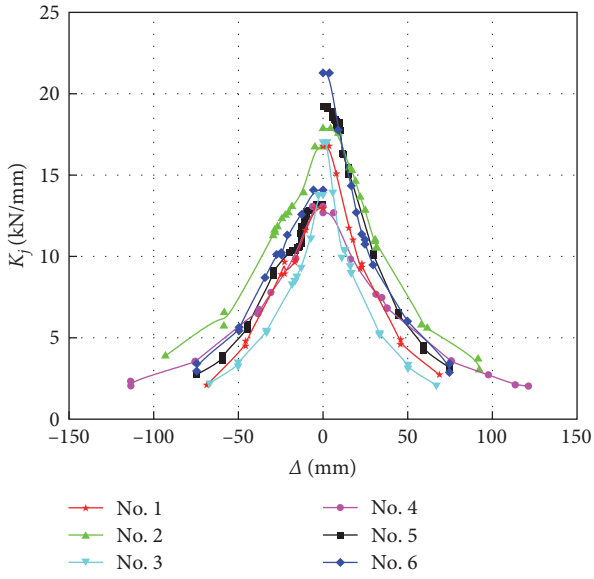

Figure 11: Curves of the stiffness degradation of $K_j-\Delta$.

yield point (K_m/K_y), and the ratio of the stiffness between plastic and yield point (K_p/K_y). The K_p/K_y ranged from 0.68 to 0.91. The K_m/K_y ranged from 0.37 to 0.85.

3.5. Ductility and Energy Dissipation Capacity. Energy dissipation (E) in each cycle and accumulated energy dissipation (E_a) of each square CFST column are both exhibited in Figure 12. When Δ was less than 20 mm, six specimens were in the elastic deformation phase. After $\Delta = 20$ mm, the energy dissipation increased gradually.

With the width–thickness ratio decreased, the energy dissipation capacities in columns No. 1, No. 6, and No. 2 improved gradually. Compared with Specimen No. 3 and No. 6, a small slenderness ratio could improve the energy dissipation capacities. Among No. 4–No. 6, the cumulative energy dissipation of No. 5 was the lowest, and No. 4 dissipated the most energy. It indicates that reducing the axial

Table 5: K_y, K_p, K_m, K_p/K_y, and K_m/K_y.

Specimen	Loading direction	K_y	K_p	K_m	K_p/K_y	K_m/K_y
No. 1	Positive	11.34	9.70	5.12	0.86	0.45
	Negative	9.12	8.15	5.04	0.89	0.55
No. 2	Positive	13.61	12.01	5.62	0.88	0.41
	Negative	11.63	10.54	5.74	0.91	0.49
No. 3	Positive	7.67	6.78	2.87	0.88	0.37
	Negative	6.76	5.11	3.09	0.76	0.46
No. 4	Positive	7.56	6.34	3.21	0.84	0.42
	Negative	8.31	6.99	3.65	0.84	0.44
No. 5	Positive	15.65	10.7	9.63	0.68	0.62
	Negative	9.64	8.25	7.95	0.86	0.82
No. 6	Positive	14.91	10.87	6.06	0.73	0.41
	Negative	10.15	9.03	8.59	0.89	0.85

compression ratio could improve the energy consumption capacities.

The equivalent viscous damping coefficient (ξ_{eq}) is assessed by Equation (4). Figure 13(a) shows the calculation diagram.

$$\xi_{eq} = \frac{1}{2\pi} \cdot \frac{S_{ABCD}}{S_{OBF} + S_{ODE}}, \tag{4}$$

where S_{ABCD} represents the cycle area on the hysteresis curves; S_{OBF} and S_{ODE} represent the area of triangles OBF and ODE, separately.

With the displacement increasing, the coefficient ξ_{eq} generally increased (Figure 13(b)). The ξ_{eq} corresponding to the plastic point ($\xi_{eq,p}$), yield point ($\xi_{eq,y}$), and ultimate point ($\xi_{eq,u}$) are exhibited in Table 6. Coefficients $\xi_{eq,y}$, $\xi_{eq,p}$, and $\xi_{eq,u}$ were in a range of 0.078–0.131, 0.084–0.159, and 0.321–0.384, respectively.

$$\mu = \frac{\Delta_u}{\Delta_y}, \tag{5}$$

where Δ_y and Δ_μ represent the yield and ultimate displacement, separately.

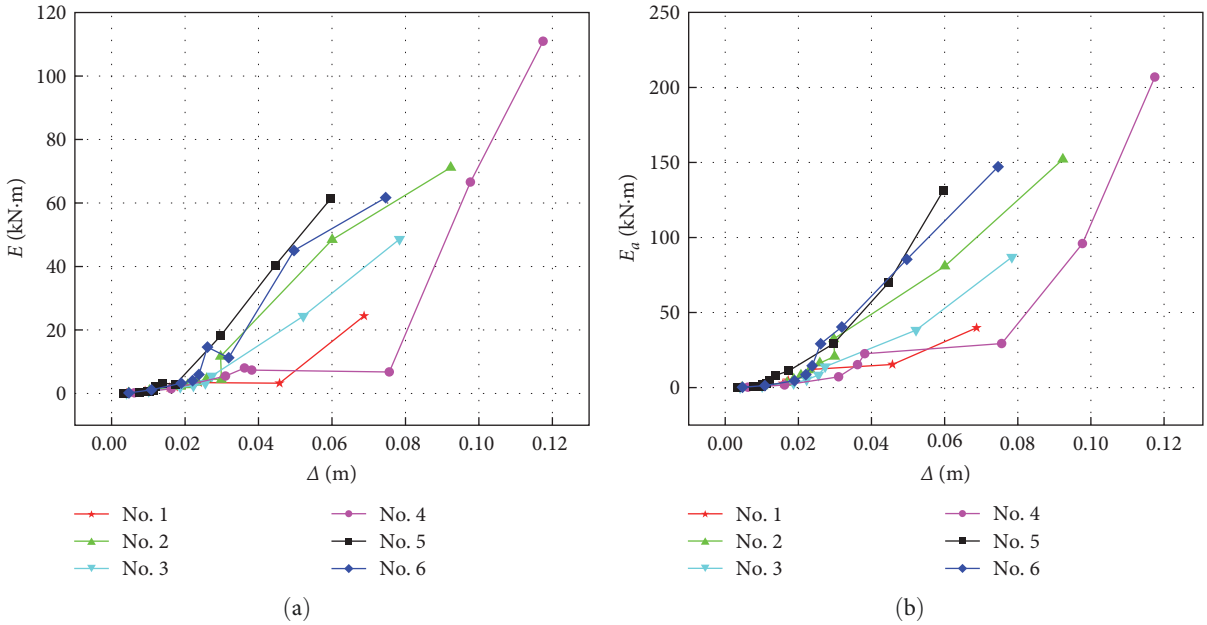

Figure 12: Various energy quantities versus displacement of each specimen: (a) $E-\Delta$ curves and (b) $E_a-\Delta$ curves.

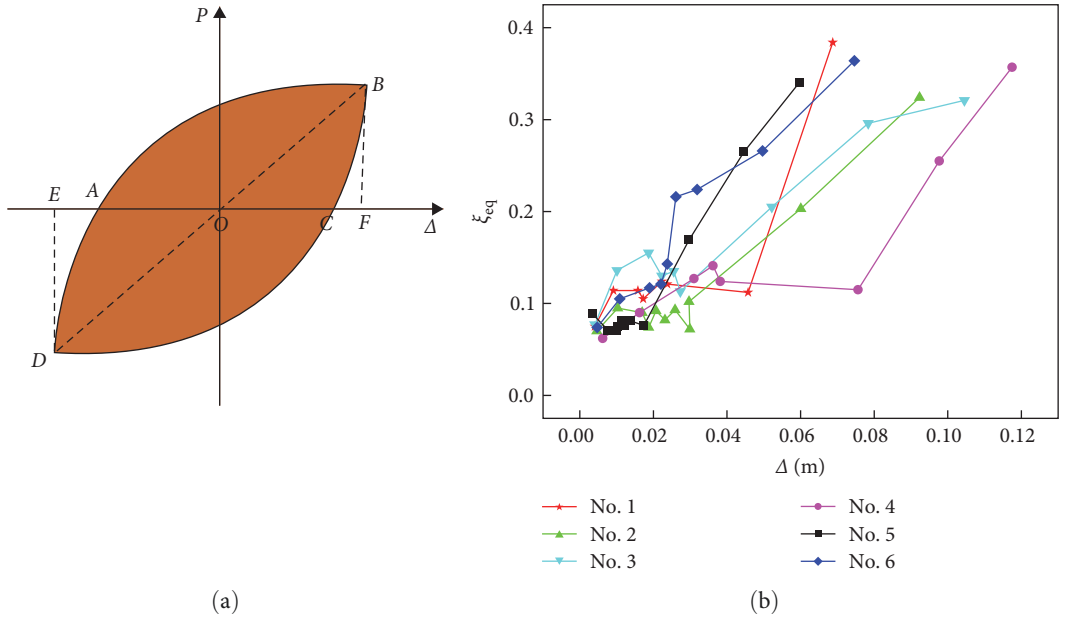

Figure 13: ξ_{eq} of specimens: (a) calculation diagram and (b) $\xi_{eq}-\Delta$ curves.

Table 6: ξ_{eq} at characteristic points.

Specimen	$\xi_{eq,y}$	$\xi_{eq,p}$	$\xi_{eq,u}$
No. 1	0.108	0.121	0.384
No. 2	0.083	0.084	0.324
No. 3	0.129	0.133	0.321
No. 4	0.131	0.136	0.357
No. 5	0.078	0.153	0.340
No. 6	0.112	0.159	0.364

Table 7: Ductility factor μ for specimens.

Specimen	No. 1	No. 2	No. 3	No. 4	No. 5	No. 6
μ	2.988	2.977	3.981	3.192	4.263	2.984

The ductility coefficient (μ) of six specimens ranged from 2.98 to 4.26 (Table 7). It indicates that all specimens exhibit excellent ductility.

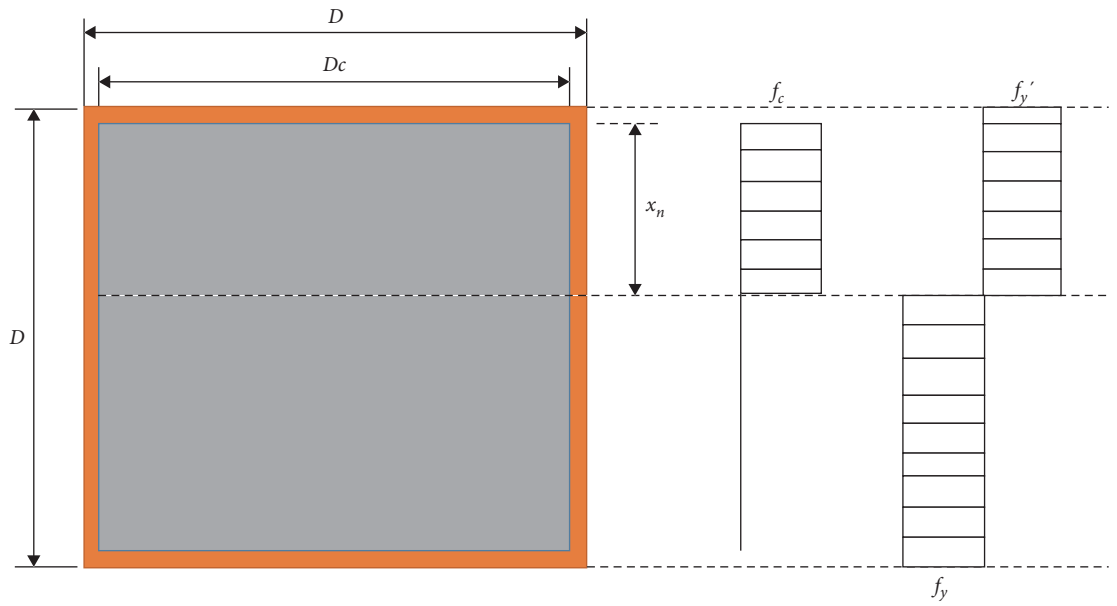

Figure 14: Stress distribution of the CFST column.

4. Calculate

4.1. Calculation Formula. The ultimate moment strength of square CFST columns was assessed according to the limit equilibrium theory. The section of CFST columns is composed of the concrete portion and steel tube. The full section yield criterion was adopted. While, the tensile contribution of concrete was ignored. The ultimate bending strength is defined in Figure 14.

$$N_u = N_{u,C} + N_{u,T}, \tag{6}$$

$$N_{u,C} = f_c \cdot x_n \cdot D_c, \tag{7}$$

$$N_{u,T} = \sum_i f'_{yi} \cdot A'_{si} - \sum_j f_{yj} \cdot A_{sj}, \tag{8}$$

$$M_u = M_{u,C} + M_{u,T}, \tag{9}$$

$$M_{u,C} = f_c \cdot x_n \cdot D_c \cdot 0.5\,(D_c - x_n), \tag{10}$$

$$M_{u,T} = \sum_i f'_{yi} \cdot A'_{si} \cdot r_i + \sum_j f_{yj} \cdot A_{sj} \cdot r_j, \tag{11}$$

where A_{si}' and f_{yi}' represent the area and yield strength of the i-th compressed steel plate, separately; A_{si} and f_{yi} represent the area and yield strength of the j-th tensile steel plate, separately; r_i and r_j represent spacing between the i-th compressed steel plate and the j-th tensile steel plate to the centroid axis, respectively; x_n represent the height of the concrete compression area.

4.2. Results Comparison. The *N-M* interaction curves of six columns are exhibited in Figure 15. Table 8 compares their maximum moments obtained by calculation ($M_{\max,C}$) and test ($M_{\max,T}$). The ratio of the maximum moment between the test and calculation ($M_{\max,T}/M_{\max,C}$) ranged from 0.93 to 1.11. The average of $M_{\max,T}/M_{\max,C}$ was 1.03 and the variation coefficient was 0.057. The results indicated that the proposed calculating method could accurately evaluate the bearing capacities of square CFST columns.

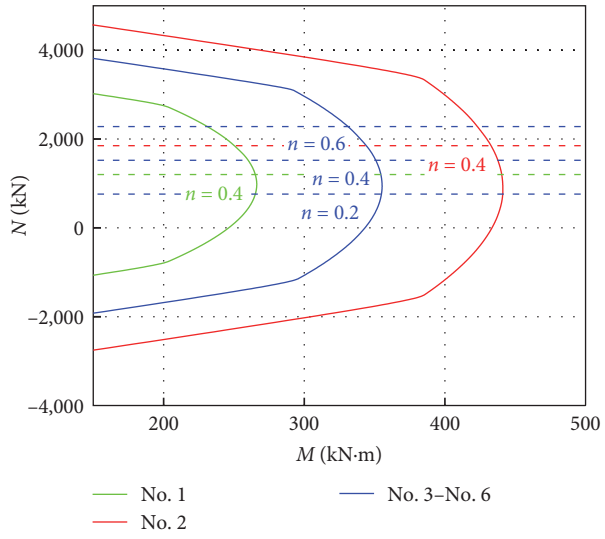

Figure 15: *N–M* curves.

Table 8: Comparison between the tested and calculated results.

Specimen	$M_{\max,\ C}$	$M_{\max,\ T}$	$M_{\max,\ T}/M_{\max,\ C}$
No. 1	266	277	1.04
No. 2	433	459	1.06
No. 3	353	366	1.04
No. 4	354	328	0.93
No. 5	331	367	1.11
No. 6	353	359	1.02

5. Conclusion

The paper studies the effects of width–thickness ratio (D/t), axial compression ratio (n), and slenderness ratio (λ) on the cyclic behavior of the square CFST columns under the cyclic loading. The bending capacity was evaluated by the proposed calculation method. The primary conclusions are summarized as follows:

(1) A bigger D/t would weaken the energy dissipation capacities and bearing capacities of the CFST columns but has little effect on ductility.

(2) With an increased λ, the energy dissipation capacities and bearing capacities of CFST columns decreased, and the stiffness of the columns deteriorated rapidly.

(3) As the n increasing, the bearing capacities of CFST columns could be intensified but the energy dissipation capacities and the stiffness would be weakened.

(4) The ultimate moment strength of the square CFST columns was assessed according to the limit equilibrium theory. $M_{\max,T}/M_{\max,C}$ ranged from 0.93 to 1.11. The average of $M_{\max,T}/M_{\max,C}$ was 1.03, and the coefficient of variation was 0.057. The proposed calculation method could accurately predict the bearing capacities of CFST columns.

Data Availability

The datasets generated or analyzed during this study are available from the corresponding author on reasonable request.

Conflicts of Interest

The authors declare that they have no conflicts of interest.

Acknowledgments

This work was supported by Shandong Provincial Natural Science Foundation, China (grant no. ZR2020ME241); Shandong Provincial Natural Science Foundation, China (grant no. ZR2021ME004); Shandong Housing and Urban Rural Construction Science and Technology Plan Project, China (grant no. 2020-K4-12).

References

[1] L.-H. Han, W. Li, and R. Bjorhovde, "Developments and advanced applications of concrete-filled steel tubular (CFST) structures: members," *Journal of Constructional Steel Research*, vol. 100, pp. 211–228, 2014.

[2] C. Ibañez, D. Hernández-Figueirido, and A. Piquer, "Shape effect on axially loaded high strength CFST stub columns," *Journal of Constructional Steel Research*, vol. 147, pp. 247–256, 2018.

[3] Z.-B. Wang, Z. Tao, L.-H. Han, B. Uy, D. Lam, and W.-H. Kang, "Strength, stiffness and ductility of concrete-filled steel columns under axial compression," *Engineering Structures*, vol. 135, pp. 209–221, 2017.

[4] F.-X. Ding, J. Liu, X.-M. Liu, Z.-W. Yu, and D.-W. Li, "Mechanical behavior of circular and square concrete filled steel tube stub columns under local compression," *Thin-Walled Structures*, vol. 94, pp. 155–166, 2015.

[5] F.-X. Ding, J. Zhu, S. S. Cheng, and X. Liu, "Comparative study of stirrup-confined circular concrete-filled steel tubular stub columns under axial loading," *Thin-Walled Structures*, vol. 123, pp. 294–304, 2018.

[6] S.-H. Lee, Y.-H. Choi, Y.-H. Kim, and S.-M. Choi, "Structural performance of welded built-up square CFST stub columns," *Thin-Walled Structures*, vol. 52, pp. 12–20, 2012.

[7] B. Evirgen, A. Tuncan, and K. Taskin, "Structural behavior of concrete filled steel tubular sections (CFT/CFSt) under axial compression," *Thin-Walled Structures*, vol. 80, pp. 46–56, 2014.

[8] Y. Yang, C. Wu, Z. Liu, Y. Qin, and W. Wang, "Comparative study on square and rectangular UHPFRC-Filled steel tubular (CFST) columns under axial compression," *Structures*, vol. 34, pp. 2054–2068, 2021.

[9] P. Ayough, Z. Ibrahim, N. H. R. Sulong, and P.-C. Hsiao, "The effects of cross-sectional shapes on the axial performance of concrete-filled steel tube columns," *Journal of Constructional Steel Research*, vol. 176, Article ID 106424, 2021.

[10] O. A. Qasim, "Numerical investigation analysis of variables effect on composite concrete filled steel tube columns," *AIP Conference Proceedings*, vol. 2213, Article ID 020195, 2020.

[11] J.-R. Qian and Z. Jiang, "Calculation method for axial compressive strength of steel tube-reinforced concrete composite columns," *Engineering Mechanics*, vol. 28, no. 4, pp. 49–57, 2011.

[12] X.-J. Ke, Z.-P. Chen, J.-Y. Xue, and Y.-S. Su, "Experimental study on the bearing capacity of recycled aggregate concrete-filled square steel tube short columns under axial compression," *Engineering Mechanics*, vol. 30, no. 8, pp. 35–41, 2013.

[13] X. Zhang and X. Gao, "The hysteretic behavior of recycled aggregate concrete-filled square steel tube columns," *Engineering Structures*, vol. 198, Article ID 109523, 2019.

[14] A. Silva, Y. Jiang, J. M. Castro, N. Silvestre, and R. Monteiro, "Monotonic and cyclic flexural behaviour of square/rectangular rubberized concrete-filled steel tubes," *Journal of Constructional Steel Research*, vol. 139, pp. 385–396, 2017.

[15] Y.-T. Wang, J. Cai, and Y.-L. Long, "Hysteretic behavior of square CFT columns with binding bars," *Journal of Constructional Steel Research*, vol. 131, pp. 162–175, 2017.

[16] Z. Chen, C. Jing, J. Xu, and X. Zhang, "Seismic performance of recycled concrete-filled square steel tube columns," *Earthquake Engineering and Engineering Vibration*, vol. 16, pp. 119–130, 2017.

[17] Z. Zhou, D. Gan, M. D. Denavit, and X. Zhou, "Seismic performance of square concrete-filled steel tubular columns with diagonal binding ribs," *Journal of Constructional Steel Research*, vol. 189, Article ID 107074, 2022.

[18] J.-J. Xu, Z.-P. Chen, J.-Y. Xue, Y.-L. Chen, and J.-T. Zhang, "Simulation of seismic behavior of square recycled aggregate concrete-filled steel tubular columns," *Construction and Building Materials*, vol. 149, pp. 553–566, 2017.

[19] R. Han, H. Zhao, Y. Sun, N. Ju, and S. Zhao, "Cyclic behavior of concrete-filled square tubular columns with stiffened plastic hinge region," *Journal of Constructional Steel Research*, vol. 190, Article ID 107152, 2022.

[20] X. J. Ke, Y. S. Su, and X. Y. Shang, "Strength calculation and eccentric compressive test of steel tube-reinforced concrete composite columns," *Engineering Mechanics*, vol. 35, no. 12, pp. 134–142, 2018.

[21] B. Mou, W. Zhou, Q. Qiao, P. Feng, and C. Wu, "Column base joint made with ultrahigh-strength steel bars and steel tubular: an experimental study," *Engineering Structures*, vol. 228, Article ID 111483, 2021.
[22] Q.-Y. Qiao, W.-W. Zhang, B. Mou, and W.-L. Cao, "Seismic behavior of exposed concrete filled steel tube column bases with embedded reinforcing bars: experimental investigation," *Thin-Walled Structures*, vol. 136, pp. 367–381, 2019.
[23] "GB/T 228.1-2010, metallic materials—tensile testing—Part 1: method of test at room temperature," Standards Press of China, Beijing, 2010.
[24] "GB/T50081-2002, standard for method of mechanical properties on ordinary concrete," China Building Industry Press, Beijing, 2002.
[25] "JGJ/T 101-2015, specification for seismic test of buildings," China Building Industry Press, Beijing, 2015.